

# UCSF

## UC San Francisco Previously Published Works

### Title

TOPAS-imaging: extensions to the TOPAS simulation toolkit for medical imaging systems.

### Permalink

<https://escholarship.org/uc/item/5q85w67m>

### Journal

Physics in Medicine & Biology, 68(8)

### Authors

Lee, Hoyeon  
Cheon, Bo-Wi  
Feld, Joseph  
[et al.](#)

### Publication Date

2023-04-03

### DOI

10.1088/1361-6560/acc565

Peer reviewed



Published in final edited form as:

*Phys Med Biol.* ; 68(8): . doi:10.1088/1361-6560/acc565.

## TOPAS-imaging: Extensions to the TOPAS simulation toolkit for medical imaging systems

Hoyeon Lee<sup>1</sup>, Bo-Wi Cheon<sup>2</sup>, Joseph W. Feld<sup>3</sup>, Kira Grogg<sup>4</sup>, Joseph Perl<sup>5</sup>, José A. Ramos-Méndez<sup>6</sup>, Bruce Faddegon<sup>6</sup>, Chul Hee Min<sup>2</sup>, Harald Paganetti<sup>1</sup>, Jan Schuemann<sup>1</sup>

<sup>1</sup>Department of Radiation Oncology, Massachusetts General Hospital and Harvard Medical School, Boston, MA 02114, USA

<sup>2</sup>Department of Radiation Convergence Engineering, Yonsei University, Wonju, Gangwon-do 26493, Republic of Korea

<sup>3</sup>Electrical Engineering and Computer Science Department, Massachusetts Institute of Technology, Cambridge, MA 02139, USA

<sup>4</sup>The Gordon Center for Medical Imaging, Department of Radiology, Massachusetts General Hospital and Harvard Medical School, Boston, MA 02114, USA.

<sup>5</sup>SLAC National Accelerator Laboratory, Menlo Park, CA 94025 USA.

<sup>6</sup>Department of Radiation Oncology, University of California San Francisco, San Francisco, CA 94115 USA.

### Abstract

**Objective:** The TOOl for PArticle Simulation (TOPAS) is a Geant4-based Monte Carlo software application that has been used for both research and clinical studies in medical physics. So far, most users of TOPAS have focused on radiotherapy-related studies, such as modeling radiation therapy delivery systems or patient dose calculation. Here, we present the first set of TOPAS extensions to make it easier for TOPAS users to model medical imaging systems.

**Approach:** We used the extension system of TOPAS to implement pre-built, user-configurable geometry components such as detectors (*e.g.*, flat-panel and multi-planar detectors) for various imaging modalities and pre-built, user-configurable scorers for medical imaging systems (*e.g.*, digitizer chain).

**Main Results:** We developed a flexible set of extensions that can be adapted to solve research questions for a variety of imaging modalities. We then utilized these extensions to model specific examples of cone-beam CT (CBCT), positron emission tomography (PET), and prompt gamma (PG) systems. The first of these new geometry components, the FlatImager, was used to model example CBCT and PG systems. Detected signals were accumulated in each detector pixel to obtain the intensity of X-rays penetrating objects or prompt gammas from proton-nuclear interaction. The second of these new geometry components, the RingImager, was used to model an example PET system. Positron-electron annihilation signals were recorded in

crystals of the RingImager and coincidences were detected. The simulated data were processed using corresponding post-processing algorithms for each modality and obtained results in good agreement with the expected true signals or experimental measurement.

**Significance:** The newly developed extension is a first step to making it easier for TOPAS users to build and simulate medical imaging systems. Together with existing TOPAS tools, this extension can help integrate medical imaging systems with radiotherapy simulations for image-guided radiotherapy.

## Keywords

Monte Carlo; medical imaging; cone-beam CT; positron emission tomography; prompt gamma

---

## 1. INTRODUCTION

In radiation applications, Monte Carlo techniques are commonly used to simulate real-world experiments. Several MC toolkits and applications have been developed to support various geometry modeling and scoring functions (Agostinelli *et al* 2003, Rogers *et al* 1995, Battistoni *et al* 2007, Forster *et al* 2004). Among these, Geant4 is a general-purpose toolkit with well-established physics models, which has been widely used in medical applications (Sardari *et al* 2010, Spiga *et al* 2007, Ahmed *et al* 2020). However, comprehensive programming knowledge is required to build and run simulations using Geant4. To reduce the programming burden, the TOol for PARTicle Simulation (TOPAS) (Perl *et al* 2012, Faddegon *et al* 2020) was developed. TOPAS wraps and extends Geant4, providing a pre-built application that users can configure for a variety of medical physics simulations without the user needing to know any C++ or other programming languages. TOPAS includes a wide variety of pre-built, using configurable geometry components and scorers for common applications in radiotherapy, configurable via text-based input files, called TOPAS Parameter Control Files. TOPAS further offers an extension system, with which individual users or teams can create and share additional C++ code to extend TOPAS functionality, to implement additional geometry components, scorers, particle sources and more. This extension system has already been used to add biological effectiveness calculation (Polster *et al* 2015), microdosimetry (Zhu *et al* 2019), as well as the extensive TOPAS-nBio tool for cellular and sub-cellular Monte Carlo biology (Schuemann *et al* 2018),

TOPAS has been widely adopted for simulating radiotherapy applications for both clinical and research purposes. Medical imaging is another major radiation application in medicine. Imaging devices based on ionization radiation are widely used in clinical practice to diagnose patients, delineate organ and tumor, and verify patient positioning for treatment. MC simulation is essential to design, optimize, and validate such imaging systems. Therefore, there have been efforts to develop dedicated MC codes for specific imaging systems or model various systems using general-purpose MC packages (Salvadori *et al* 2020, Assié *et al* 2004, Paredes-Pacheco *et al* 2021, Badal and Badano 2009, Harrison *et al* 1993). GATE (Jan *et al* 2004) and GAMOS (Arce *et al* 2008) are Geant4-based MC codes, which have been used to model various ionizing radiation-based imaging systems and radiotherapy. There are also MC codes dedicated to modeling specific imaging modalities to improve computational efficiency with simplified physics model and hardware acceleration,

*e.g.*, SimPET (Paredes-Pacheco *et al* 2021) for PET simulation, MCGPU (Badal and Badano 2009) for CBCT simulation, and MCGPU-VICTRE (Badal *et al* 2021) for mammography and digital breast tomosynthesis simulation. For each of these other MC tools, a user who wishes to make more than a limited set of pre-defined changes to the system they are modeling must make their changes on the C++ or Fortran level, writing, compiling, and linking their new code. In contrast, TOPAS users can model whole new systems without programming expertise, just writing or modifying TOPAS Parameter Control Files.

The aim of this study is to develop a set of TOPAS extensions to further expand the flexible modeling of medical imaging systems.

## 2. Methods and Materials

### 2.A. Code structure

TOPAS-imaging is a set of TOPAS extensions including new Geometry Components and Scorers which are in turn based on TOPAS core classes. The schematic diagram in Figure 1 presents class hierarchy of TOPAS-imaging in unified modeling language (UML) format, which is a standard way to describe hierarchy of classes in object-oriented programming. The key aspects of UML used here are as follows: Solid black arrows depict the inheritance relationship between two classes. Dashed diamond arrows depict composite relationship between classes, which means a class object is used in the other class. A class connected and pointed to by the arrow inherits from a class or uses a class object on the other end of the arrow. For example, the DigitizerScorer inherits TsNTuple class, and uses Pulse object and digitizers in the member functions of the class.

The new geometry component classes we provide are RingImager and FlatImager. These inherit from a more generic imager geometry class, Imager, that handles parameters that are common to all imaging detectors. Imager then inherits from the TOPAS geometry base class, TsVGeometryComponent. The geometry component class relationship is shown in Figure 1 (a). The new scorer classes we provide are PETScorer, SPECTScorer, and PGScorer. These inherit from a more generic digitizer scorer class, DigitizerScorer, which inherits from the TOPAS scoring base class, TsNTuple. The digitizer scorer handles detected signals using the pulse class (Pulse), which stores detected signals in a tuple, and builds a sequence of digitizers (digitizer chain) that inherits from the digitizer class (Digitizer), as shown in Figure 1 (b). For CBCT scoring, we implemented a separate scorer class CBCTScorer, which inherits from the TOPAS scoring base class, TsVBinnedScorer. CBCTScorer acquires 2D projection data, and includes variance reduction functions specific to CT imaging, *i.e.*, optical spread function and forced interaction, as shown in Figure 1 (c).

### 2.B. Detector Geometry

**2.B.1 Flat-panel detector**—Flat-panel detectors are widely used for radiation detection in imaging, such as CBCT. They are typically composed of a buildup layer, an array of scintillating crystals, and a photodetector in general. In such a detector, the photons interact with scintillating crystals in the detector, and the created optical photons are detected in the photodetector. We built a user-configurable flat-panel detector with a columnar scintillator

layer (Miller *et al* 2005, Bugby *et al* 2016). Users can configure the size and material of the scintillators and the reflective substance via TOPAS parameters. A schematic diagram of a flat-panel detector is shown in Figure 2 (a) and (b). In the figure, the gray-colored cylinders depict scintillating materials and red circles depict reflective material covering the scintillator. An example TOPAS Parameter Control File to configure this geometry component is shown in Figure 2 (c). The setup of the simulation for the whole geometry requires only a few parameters to be set, including the size and material of each layer. The parameters build a CBCTImager, which is composed of a carbon buildup layer (Prefilters), a scintillation layer (Crystal), and a photodetector layer (PhotoDetector). The Crystal/Shape, Crystal/Radius, Crystal/HL, Crystal/ReflectorThickness, Crystal/ReflectorMaterial, and Crystal/Material characterize the shape of crystals, radius of crystal cylinders, length of crystal cylinders, the thickness of reflective material, reflective material, and crystal material, respectively. The geometry component can also be configured to model rectangular crystals by toggling the shape into Box. The Crystal/HLX, Crystal/HLY, and Crystal/HLZ will be used to characterize the length of each axis of the crystals for rectangular crystals. The Crystal/XGap and Crystal/ZGap define spaces between each crystal. The extent of CBCTImager is calculated by the extension to cover the crystals and the gaps.

**2.B.2 Ring-shaped detector**—Ring-shaped detectors are widely used for PET and SPECT systems. The ring is composed of multiple detectors that face towards a central axis to detect signals coming from inside the field-of-view (FOV) of the detector. Clinical PET systems typically have a hierarchical construction (Lu *et al* 2016, Grogg *et al* 2016). In our design, the construction hierarchy is composed of detectors, modules, submodules, and crystals as shown in Figure 3 (a). The user has full flexibility to configure the size and the number of divisions in each layer of the hierarchy. An example TOPAS Parameter Control File to configure this geometry component for a PET system is shown in Figure 3 (b). As for the flat panel detector, the material of the crystal is configured by the parameters Crystal/Material. The size of each crystal is controlled by the parameters Crystal/HLX, Crystal/HLY, and Crystal/HLZ. We assumed that the crystals are placed in a grid form in the submodules and the number of crystals in each axis is defined by the parameters Crystal/NbOfXBins, Crystal/NbOfYBins, Crystal/NbOfZBins. The gaps between each crystal are defined by Crystal/XGap and Crystal/ZGap. The number of submodules per module, modules per detector, and detectors are controlled by the parameters Submodule/NbOf\*Bins, Module/NbOf\*Bins, and NbOfDetectors, respectively. Users can configure the space between each module and each submodule using the parameter Module/\*Gap and Submodule/\*Gap, respectively. The size of the submodules, modules, and detectors are calculated internally using the size, number, and gap of subdivisions.

**2.B.3 Parallel hole collimator**—Collimators are used in medical imaging detection systems to remove scattered radiation and improve spatial resolution (Audenhaege *et al* 2015, Alexeev *et al* 2018, Lopes *et al* 2012). We implemented a rectangular parallel holes collimator array as a subcomponent for SPECT and PG imaging systems. The collimator can be enabled within the above Imager geometry component by toggling the parameter Collimator/Exists to True as shown in Figure 3 (b). The collimator subcomponent is built onto the front of the detector crystal. The X and Z extent of the collimation

surface is automatically scaled to match the X and Z extent of the Imager. The depth of the collimator is set via the parameter Collimator/HL. The parameters Collimator/XSeptaThicknessPercentage and Collimator/ZSeptaThicknessPercentage define the ratio of wall thicknesses of collimator over crystal sizes. The number of collimator holes along X- and Z-axes will match the Crystal/NbOfXBins and Crystal/NbOfZBins in the Imager, respectively. The volume of the collimator hole, marked as blue in Figure 4, is filled with materials configured by the parameter Collimator/OpeningMaterial (default is Air) while the collimator material is set using Collimator/Material.

## 2.C. Scorers

Any already existing TOPAS scorer can be used with the new geometry extensions we described. One can, for example, score energy deposition, fluence, phase space, etc. in any of the above new geometry components. However, some aspects of imaging system research require more specialized forms of output. To this this end, TOPAS-imaging adds additional TOPAS scoring extensions described below.

**2.C.1 CBCTScorer**—The signal from a CBCT is scored from the optical photons created by the interaction between X-ray and the scintillating materials. The energy of the optical photons is accumulated in the photodetector to obtain projection data. Users can define the optical properties of the scintillating material to generate optical photons and the optical properties of the region between the scintillator and photodetectors to transport and detect optical photons. Supported optical surface properties in TOPAS can be found in the user guide (<https://topas.readthedocs.io/en/latest/>).

While simulating the transportation and detection of optical photons accurately represents the detection processes in a CBCT detector, modeling optical photons requires a large amount of computation time as several thousand optical photons are created per interaction in the scintillators. To improve the efficiency of the simulation, we implemented 2 variance reduction techniques. One is numerical modeling of the optical photon transportation. To implement the numerical modeling, users need measurements of the optical spread function, i.e., the energy deposition efficiency for mono-energetic photons in the detector and diffusion of the optical photons in the small subsets of the detector (Shi *et al* 2019, O’Connell and Bazalova-Carter 2021). The forced interaction technique (García-Pareja *et al* 2021) was implemented to further improve computational efficiency. Every photon entering the detector is forced to be converted into optical photons, and the optical spread function is accumulated without random rejection with the forced interaction technique. The accumulated optical spread function is scaled with an appropriate weight to maintain the level of detected signals when forced interaction is used. The optical spread function allows using a simplified scintillator geometry (Shi *et al* 2019) since the physics processes inside the scintillator are replaced by a point spread function.

The CBCT scorer was implemented based on the binned scorer in TOPAS. Therefore, scoring results can be saved in any file format supported by TOPAS, i.e., binary, DICOM, or csv. Also, users can utilize functionalities offered for scoring in TOPAS, such as binning or filter to simulate an energy resolving detectors or distinguish primary and scattered photons.

**2.C.2 PETScorer**—PET system detects pairs of photons from electron-positron annihilation, typically using a ring-shaped detector. Detected signals are digitized and paired into coincidence as shown in Figure 5. Each detected signal is called a hit, and the remaining signals after all the digitization are called singles (Jan *et al* 2004).

We implemented 6 different digitizer modules: adder, energy cutoff, timing resolution, dead-time, sigmoidal threshold, and pulse pile-up. In the simulation, a photon may interact with a crystal multiple times until it is completely absorbed. The adder module accumulates the energy deposition of a photon in a crystal. The energy cutoff module removes the detected signals outside the user-defined energy window. The timing resolution module randomly shifts the detected time, the dead-time module ignores signals detected in the user-defined dead-time of the crystal, and the sigmoidal threshold module generates a random number and rejects hits if the random number is larger than a threshold. The pulse pile-up module only accepts the last hit in the crystal within the temporal window.

To detect coincidence pairs from the singles, users need to select 2 timing windows: a coincidence timing window and a delayed timing window. The coincidence and the delayed timing windows are the maximum temporal differences between singles to pair them as a true coincidence and random coincidence, respectively. If singles have a larger temporal difference than the delayed timing window, they are not considered as coincident signals. The coincidence detection is performed at the end of the digitizer chain after every hit goes through the digitizers, and all possible pairs of the singles in each timing window will be paired.

Currently, the extension only supports list-mode output. Each line in the output is a pair of coincidence events. The event ID of annihilation, the position of annihilation, the detected position, detector IDs, and the energy of the coincident photon are saved. Different types of output formats, such as sinogram output or binary output, will be added in the future to accommodate image reconstruction toolkits.

**2.C.3 PGScorer and SPECTScore**—The PG imaging system detects PGs generated in proton-induced nuclear interactions using a flat-panel detector or Compton camera. The PGs of energies few MeV are emitted in nanoseconds scale after protons interact with matter (Wro ska 2020). The SPECT system detects gamma rays from radioactive decay using multiple gamma cameras. The energies of the gamma rays used for the SPECT imaging vary depending on radioisotopes, typically around 100 to 300 keV (Cri an *et al* 2022, Bouziotis *et al* 2013). Though the PG and SPECT systems detect different particles with different types of detectors, they both utilize digitizers in the detection process, similar to PET, to eliminate unwanted signals. The PGScorer and SPECTScorer follow a chain similar to that shown in Figure 5, except for the coincidence detection step. These scorers currently only support list-mode output. Specifically, they output the accumulated signal per each detector pixel.

## 2.D. Example cases

To demonstrate the TOPAS-imaging extensions, we modeled example cases for CBCT, PET and PG systems, and phantoms for each image acquisition to showcase how the extension can be used and extended. The CBCT and PG imaging results were compared to the

attenuation coefficient of phantom and proton range, respectively. The PET imaging results were compared to images obtained from a brain PET system.

**2.D.1 CBCT**—The scanning geometry parameters of the example CBCT system and corresponding TOPAS parameters are summarized in Table I. In the table, the BeamPosition is a default parent component for the primary source, and the Xray is the primary X-ray source attached to the BeamPosition. We followed the X-ray tube description in Thing *et al.* (Thing *et al* 2016) and obtained energy spectra using SpekCalc (Poludniowski *et al* 2009) for a tube voltage of 120 kVp. We used both the optical spread function and forced interaction for variance reduction. The optical spread function and energy deposition efficiency were obtained for a subset of the detector of 11\*11 pixels with mono-energetic pencil beam photons between 10 keV and 120 keV in 5 keV intervals. The optical spread function and energy deposition efficiencies of photon energies not included in the simulation were obtained by linear interpolation (O’Connell and Bazalova-Carter 2021). The number of primary photons was selected to achieve an average relative standard deviation of 10~11% in log-transformed projection data.

To test image acquisition, we built a modified 3D Shepp-Logan phantom (Gach *et al* 2008), one of the widely used phantoms for numerical studies, and a contrast phantom modified from Catphan CTP 515 (The Phantom Laboratory, Greenwich, NY, USA).

The Shepp-Logan phantom is composed of ellipsoids of different sizes and materials. We assigned materials to the ellipsoids to achieve similar attenuation coefficients as the original numerical Shepp-Logan phantom and changed the positions of the ellipsoids to remove overlaps. Figure 6 (a) and (b) shows the modified Shepp-Logan phantom in top and lateral views, respectively. The color in the figure represents different materials (red: air, magenta: water, and blue: Teflon). The details of the position, size, and materials of the ellipsoids are summarized in Table II. In the original Shepp-Logan phantom, ellipsoid #3 overlaps with ellipsoids #2, #4, and #5. Though such overlaps in the geometric components can be implemented in TOPAS by writing a TOPAS extension utilizing Geant4 Boolean solids, we opted out for a simpler approach, modifying the centers of ellipsoid #2, ellipsoid #4, and ellipsoid #5, to define the phantom with standard TOPAS geometry components.

Figure 6 (c) shows the top view of the contrast phantom. The base of the phantom is a water cylinder with a radius of 75 mm and a height of 100 mm. There are 6 different insert groups with 5 different materials inside the phantom. The original Catphan CTP 515 phantom has cylindrical contrast inserts with different heights and is filled with low-contrast mimicking materials. We modified the phantom to have fixed height cylinders and replaced the materials with tissue-mimicking materials available in TOPAS. The cylinders in the outer trajectory have radii of 7.5, 4.5, 4.0, 3.5, 3.0, 2.5, 2.0, 1.5, and 1.0 mm, and the cylinders in the inner trajectory have radii of 4.5, 3.5, 2.5, and 1.5 mm.

The projection data of the CBCT were saved in binary format and reconstructed into volumetric images using the Feldkamp-Davis-Kress (FDK) algorithm (Feldkamp *et al* 1984) in the reconstruction toolkit (RTK) (Rit *et al* 2014).



**2.D.2 PET**—Using the developed extension, we built a NeuroPET/CT system (Photo Diagnostic Systems, Inc, Boxborough, MA, USA) (Grogg *et al* 2016). The details of the detector geometry, digitizer parameters, and corresponding TOPAS parameters are summarized in Table III. The PETImager is the PET detector as described in the previous section, and the PETScorer is a scorer for the PET system, which includes the digitizers and coincident detection. The dead time was set to 0 s, and the event ID in the list-mode output was used to distinguish true coincidences and random coincidences. We recorded the coordinate of annihilation origin and the detected position to identify scattered signals and remove them. The scattered signals were identified by calculating the angle between singles in each coincidence pair and removed if the angle was smaller than 172 deg. The angular difference to reject scattered signals was selected heuristically to obtain sufficient number of signals to reconstruct images. To simulate radioactive sources, we used the existing time feature in TOPAS. The type of the primary particle was set to be one of the decay products of an isotope of interest for the simulation. The number of decays at different time points was calculated by using the half-life of the isotope and the time feature to change the number of particles simulated at different time points of the simulation. The entire PET scan was divided into segments of 1 second/run, and the number of primary particles was calculated based on the initial activity. The recorded signals in a run were digitized and coincidence events were detected at the end of each run.

We investigated the sensitivity and resolution of the simulated systems and compared them with experimental results. For the sensitivity comparison, we simulated a 70 cm-long line source with an activity of 3.07 MBq for 330 seconds with 5 different thicknesses of aluminum sleeves (1.25 mm, 2.5 mm, .3.75 mm, 5 mm, and 6.25 mm). The number of detected signals was counted after converting the list-mode data into sinograms and re-binned into single-slices (Erlandsson *et al* 1994). The measurements were performed with the line source placed at the center of the FOV and 10 cm off-center in the FOV.

To measure the resolution of the system, we placed 3 PMMA encapsulated point sources in the FOV. The source has a sphere radius of 0.75 mm containing F-18 inside a PMMA cylinder, which has a height of 3.5 mm and a radius of 12 mm. Each source has an activity of 0.19 MBq, and the sources are arranged in an L-shape. The signals were collected for a simulated time of 15 minutes. We reconstructed the images using the MLEM algorithm (Shepp and Vardi 1982) with 3 iterations and applied a Gaussian filter standard deviation of 1.85 mm. The reconstructed activities were fitted with a Gaussian function, and the full-width half maximum of each Gaussian function was compared.

For quantitative comparison, we simulated the American College of Radiology (ACR)-type phantom (MacFarlane and Radiologists 2006). The phantom has a radius of 10.2 cm and a height of 18.6 cm. There are 3 different sections in the phantom to measure the resolution, uniformity, and contrast of the PET system, and it is used for quality assurance measurements at our institution. The cross-sectional slices of the contrast and resolution segments are shown in Figure 7. The red circles in the figure depict hot vials containing radioactive materials, and the blue circles depict cold rods with no radioactivity. The body of the phantom has a background activity of 13 MBq, and the cylinder-to-background ratio was set to 4:1, i.e., the hot cylinders have 4 times larger radioactivity concentration than the

background. The 3 cold rods in Figure 7 (a) are made of water, air, and Teflon from top to bottom. The rods in Figure 7 (b) are made of PMMA. We scanned the phantom for 20 minutes and converted the results into sinograms. 3D images were reconstructed using the MLEM algorithm with 100 iterations.

The list-mode data to sinogram conversion and the image reconstruction were done with the open-source software OMEGA (Wettenhovi *et al* 2021). We implemented functions to load the list-mode output from TOPAS to convert it into sinogram domain. The attenuation correction was applied for the ACR phantom image reconstruction. The voxel-wise attenuation coefficients of the phantom at 511 keV photon energy were obtained from the NIST database (Hubbell and Seltzer 2004).

**2.D.3 PG**—To demonstrate the PG imaging system, we modeled the system shown in Figure 8. A module consisting of a single PG detector with the tungsten collimator was modeled. The detector was composed of  $80 \times 32$  arrays of LYSO scintillation crystals where the unit size of each crystal was  $4.0 \times 4.0 \text{ mm}^2$ . The thickness of the scintillator was 30 mm. The tungsten collimator was attached to the detector. The dimensions and hole sizes of the collimator were  $128 \times 320 \times 300 \text{ mm}^3$  and  $3.2 \times 3.2 \text{ mm}^2$ , respectively, and the septal wall thickness between the holes was 0.4 mm. A water phantom size of  $128 \times 128 \times 320 \text{ mm}^3$  was located at a 10 cm distance from the collimator surface. To improve computational efficiency of the simulation, we utilized phase space source in TOPAS. We obtained phase spaces for proton energy of 150 MeV and 200 MeV using TOPAS. The phase spaces of prompt gamma were recorded using a cylinder surrounding the water phantom with  $10^9$  primary proton particles. For both energies of proton beams, the primary source has offsets of 15 mm in both horizontal and vertical directions. We sampled  $5^7$  prompt gammas from the phase space to simulate PG imaging. We used the cutoff digitizer to detect PGs with energies of 3–5 MeV. The simulations were done with a stationary PG detector and rotating detector. For the rotating detector case, we used the time feature in TOPAS to rotate the detector around the isocenter for a 1-degree angular interval to obtain prompt gamma signals in different angular positions and the number of prompt gamma was equally distributed to each angular sampling. The measured data with rotating detector were reconstructed using the MLEM algorithm in CASToR (Merlin *et al* 2018).

### 3. Results and Discussion

The simulations were performed with high performance computing environment at our institution equipped with Intel Xeon CPUs.

#### 3.A. CBCT

Figure 9 shows the projection data obtained from the simulation for the modified Shepp-Logan phantom at 0 deg and 90 deg rotation. The central slice of the numerical phantom and the corresponding slice in the reconstructed images are shown in Figure 10 (a) and (b), and the central horizontal and vertical line profiles are shown in Figure 10 (c) and (d). The central slice of the numerical contrast phantom and reconstructed images are shown in Figure 10 (e) and (f). Line profiles of compact bone and B-100 bone equivalent material

inserts in the phantom are plotted in Figure 10 (g) and (h). The simulation took about 5 hours per projection data with 4 CPUs.

The TOPAS-imaging extensions successfully modeled the CBCT image acquisition system and was able to reconstruct volumetric images using an FDK algorithm. We did not apply any artifact correction methods in the reconstruction process, such as scatter correction, or beam hardening correction.

The reconstructed images from the example CBCT systems show discrepancies from the ideal phantom images. This is mainly because of artifacts like angular sampling and noise. If we reduce the angular sampling ratio or increase the number of primary particles, reconstructed images will match closer. We have not compared the CBCT simulation results to a specific experimental system, but one could model systems by measuring spatial resolution and noise characteristics and optimizing geometrical parameters and the number of primary particles corresponding to scanning protocols.

### 3.B. PET

Figure 11 (a) shows the sensitivity measured from the NeuroPET/CT system compared with TOPAS simulations. Differences in sensitivity were less than 5% for all cases. The spatial resolution of the point source in the simulation was 4.10 mm at the center and 5.46 mm off-center. The resolution is slightly better than the experimental data, which has 4.24 mm at the center and 5.27 mm off-center. The reconstructed images of the ACR phantom from experimental measurement and MC simulations are shown in Figure 11 (b)–(e). The PET simulation took about 3 minutes and 1 hour on average to simulate radioactive decays per a second for the resolution phantom and the ACR phantom with a CPU, respectively.

Though we successfully measured coincident photons and reconstructed images for the spatial resolution comparison and the ACR phantoms from the simulated data, we cannot directly compare the two images quantitatively since the post-processing algorithms applied to the data and the image reconstruction algorithm used were not the same. However, qualitatively, the two images show similar behavior and accuracy.

Currently, the extension does not support multi-layer detector systems. In contrast, the experimental PET system we targeted to model uses a dual-layer detector with a different number of crystals, 21\*21 for the inner layer and 22\*22 for the outer layer. Instead, we modeled the detector to have the same number of crystals as the outer layer. Also, there are additional approximations in the digitization steps, for instance, the timing resolution of the experimental systems is unknown, and the energy resolution digitizer was not implemented.

### 3.C. PG

The data obtained from PG systems for 150 MeV and 200 MeV proton beams are shown in Figure 12 (a) and (b), respectively. As one can find in the images, most of the PGs are detected close to the proton beam path and form high intensity signals. Some of the PGs are detected away from the proton beam path and create low intensity signals in the images as they have isotropic distribution in terms of direction. Relative intensity of measured PG signals and true Bragg-peaks for 150 MeV and 200 MeV proton beams are

shown in Figure 12 (c) and (d), respectively. The measured proton range for 150 MeV from measured PG intensity was 148 mm and proton range from the Bragg peak was 154 mm. The measured range and true range for 200 MeV proton beams were 252 mm and 257 mm, respectively. Considering the size of the detector pixel is  $4 \times 4 \text{ mm}^2$ , we can locate the Bragg-peak position within a single pixel. In addition, the gaps between the estimated and true range are consistent with previously reported results obtained from Geant4 with a similar energy window (Zarifi *et al* 2017). In the reconstructed images, we could estimate the 15 mm offsets of the proton beams on both vertical and horizontal direction. The PG system simulations took about 2 minutes with 6 CPUs.

### 3.D. Advantages and Limitations

The TOPAS extension developed in this study provides predefined geometries to build detector systems and scoring functions based on the TOPAS framework. Thus, users can implement medical imaging systems without programming or develop their own geometries or scoring functions with minimal programming based on the extension system in TOPAS. Users can simulate advanced imaging systems with combinations of the developed extensions and abundant functionalities offered by TOPAS, such as binning, filtering, and 4D simulations.

The developed extensions offer fundamental components for imaging. Additional work is needed to accommodate a large variety of imaging modalities and geometry components, such as diverging or converging hole collimators, Compton cameras or gamma cameras, and digitizer modules. The development of specific imaging devices will need to be performed by users or in future work.

## 4. CONCLUSION

We introduced a set of newly developed TOPAS extensions to build imaging system geometries and score quantities for ionizing radiation-based imaging systems, CBCT, PET, SPECT, and PG. We then demonstrated our framework by building examples for CBCT, PET, and PG systems. With these extensions, complex imaging systems may be built for simulation with TOPAS by setting values for a small set of parameters. The source code for the full set of TOPAS-imaging extensions will be distributed via the GitHub repository for TOPAS-extensions (<https://github.com/topasmc/extensions>). TOPAS parameter files and image reconstruction scripts for the example cases discussed in the manuscript will be available from the TOPAS user guide (<https://topas.readthedocs.io/en/latest/>).

Radiologic imaging is a broad field with diverse imaging modalities, image reconstruction algorithms, and optimization methods. The presented framework does not intend to provide a solution to all image acquisition systems and methods. Instead, it provides fundamental functions that users can adapt and expand for their needs. We anticipate that our study will encourage TOPAS users to develop various components in medical imaging systems, for example, bowtie filters in CBCT systems to deal with patient thickness variation, PET digitizers including crosstalk or spatial blurring which are used in clinical PET systems, variance reduction methods to improve the computational efficiency, and different output formats for image reconstruction and post-processing packages.

The examples provided for demonstration and experimental validation show what can currently be done with the extension. Additional implementation and validation with clinical systems from various vendors are left to future work. We envision that users will further expand the extension and add additional features for clinical imaging applications for novel imaging systems.

## Acknowledgment

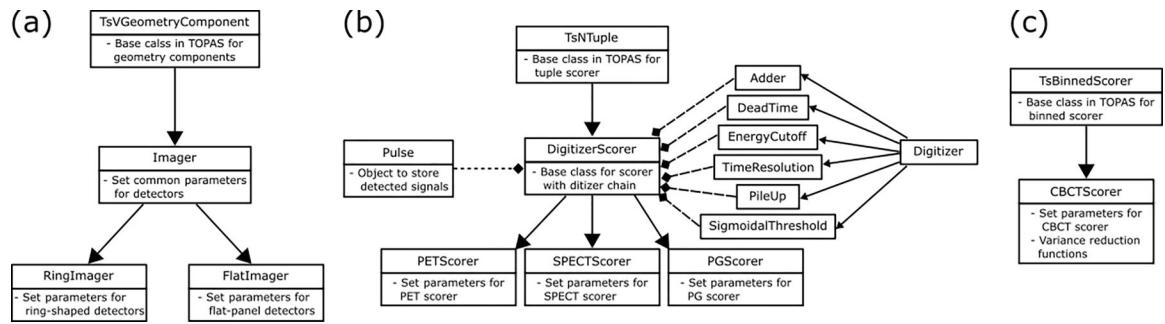
This study is supported in part by the National Cancer Institute (NIH/NCI U24 CA215123, 'The TOPAS Tool for Particle Simulation, a Monte Carlo Simulation Tool for Physics, Biology and Clinical Research'), the MIT UROP program, and the AAPM Summer student program. The authors would like to thank Sophie Longawa, Gabriel Cojocar, and Cyndy Zhang for their contribution to the implementation of the extension.

## References

- Agostinelli S, Allison J, Amako K, Apostolakis J, Araujo H, Arce P, Asai M, Axen D, Banerjee S, Barrand G, Behner F, Bellagamba L, Boudreau J, Broglia L, Brunengo A, Burkhardt H, Chauvie S, Chuma J, Chytrcek R, Cooperman G, Cosmo G, Degtyarenko P, Dell'Acqua A, Depaola G, Dietrich D, Enami R, Feliciello A, Ferguson C, Fesefeldt H, Folger G, Foppiano F, Forti A, Garelli S, Giani S, Giannitrapani R, Gibin D, Cadenas JJG, González I, Abril GG, Greeniaus G, Greiner W, Grichine V, Grossheim A, Guatelli S, Gumplinger P, Hamatsu R, Hashimoto K, Hasui H, Heikkinen A, Howard A, Ivanchenko V, Johnson A, Jones FW, Kallenbach J, Kanaya N, Kawabata M, Kawabata Y, Kawaguti M, Kelner S, Kent P, Kimura A, Kodama T, Kokoulin R, Kossov M, Kurashige H, Lamanna E, Lampén T, Lara V, Lefebvre V, Lei F, Liendl M, Lockman W, Longo F, Magni S, Maire M, Medernach E, Minamimoto K, Freitas PM de, Morita Y, Murakami K, Nagamatu M, Nartallo R, Nieminen P, Nishimura T, Ohtsubo K, Okamura M, O'Neale S, Oohata Y, Paech K, Perl J, Pfeiffer A, Pia MG, Ranjard F, Rybin A, Sadilov S, Salvo ED, Santin G, Sasaki T, et al. 2003 Geant4—a simulation toolkit Nucl Instruments Methods Phys Res Sect Accel Spectrometers Detect Assoc Equip 506 250–303
- Ahmed AM, Chacon A, Rutherford H, Akamatsu G, Mohammadi A, Nishikido F, Tashima H, Yoshida E, Yamaya T, Franklin DR, Rosenfeld A, Guatelli S and Safavi-Naeini M 2020 A validated Geant4 model of a whole-body PET scanner with four-layer DOI detectors Phys Medicine Biology 65 235051
- Alexeev T, Kavanagh B, Miften M and Altunbas C 2018 Two-dimensional antiscatter grid: A novel scatter rejection device for Cone-beam computed tomography Med Phys 45 529–34 [PubMed: 29235120]
- Arce P, Rato P, Cañadas M and Lagares JI 2008 GAMOS: A GEANT4-Based Easy and Flexible Framework for Nuclear Medicine Applications 2008 Ieee Nucl Sci Symposium Conf Rec 3162–8
- Assié K, Breton V, Buvat I, Comtat C, Jan S, Krieguer M, Lazaro D, Morel C, Rey M, Santin G, Simon L, Staelens S, Strul D, Vieira J-M and Walle R V de 2004 Monte Carlo simulation in PET and SPECT instrumentation using GATE Nucl Instruments Methods Phys Res Sect Accel Spectrometers Detect Assoc Equip 527 180–9
- Audenhaege KV, Holen RV, Vandenberghe S, Vanhove C, Metzler SD and Moore SC 2015 Review of SPECT collimator selection, optimization, and fabrication for clinical and preclinical imaging Med Phys 42 4796–813 [PubMed: 26233207]
- Badal A and Badano A 2009 Accelerating Monte Carlo simulations of photon transport in a voxelized geometry using a massively parallel graphics processing unit Med Phys 36 4878–80 [PubMed: 19994495]
- Badal A, Sharma D, Graff CG, Zeng R and Badano A 2021 Mammography and breast tomosynthesis simulator for virtual clinical trials Comput Phys Commun 261 107779
- Battistoni G, Cerutti F, Fassò A, Ferrari A, Muraro S, Ranft J, Roesler S and Sala PR 2007 The FLUKA code: description and benchmarking Aip Conf Proc 896 31–49

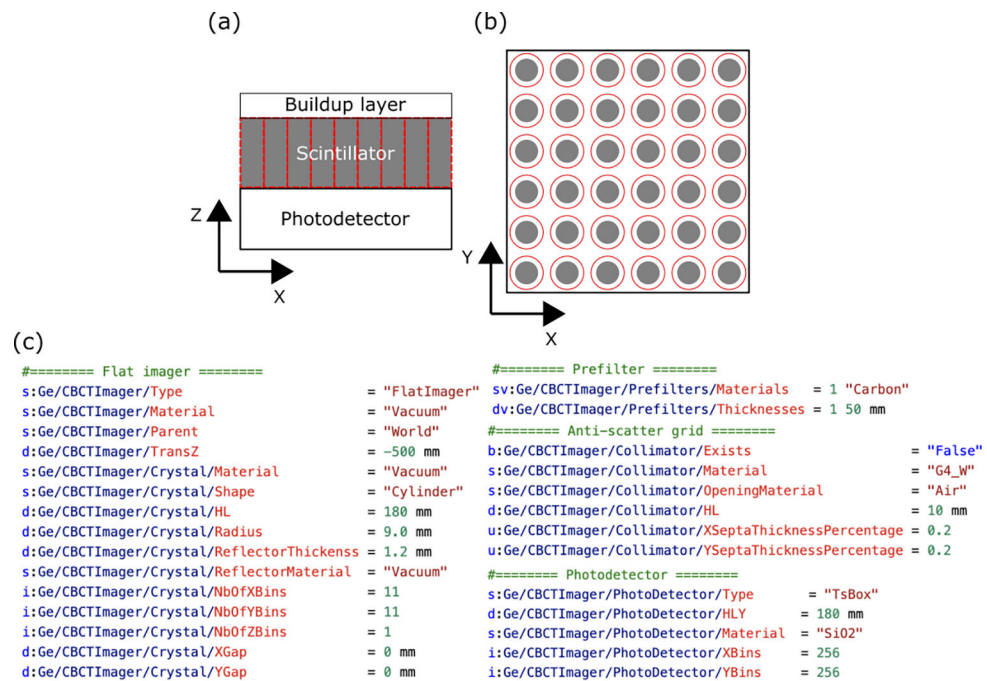
- Bouziotis P, Psimadas D, Tsotakos T, Stamopoulos D and Tsoukalas C 2013 Radiolabeled Iron Oxide Nanoparticles As Dual-Modality SPECT/MRI and PET/MRI Agents *Curr Top Med Chem* 12 2694–702
- Bugby SL, Jambi LK and Lees JE 2016 A comparison of CsI:TI and GOS in a scintillator-CCD detector for nuclear medicine imaging *J Instrum* 11 P09009
- Cri an G, Moldovean-Cioroianu NS, Timaru D-G, Andrie G, C inap C and Chi V 2022 Radiopharmaceuticals for PET and SPECT Imaging: A Literature Review over the Last Decade *Int J Mol Sci* 23 5023 [PubMed: 35563414]
- Erlandsson K, Esser PD, Strand S-E and Heertum RL van 1994 3D reconstruction for a multi-ring PET scanner by single-slice rebinning and axial deconvolution *Phys Medicine Biology* 39 619–29
- Faddegon B, Ramos-Méndez J, Schuemann J, McNamara A, Shin J, Perl J and Paganetti H 2020 The TOPAS tool for particle simulation, a Monte Carlo simulation tool for physics, biology and clinical research *Phys Medica* 72 114–21
- Feldkamp LA, Davis LC and Kress JW 1984 Practical cone-beam algorithm *Josa* 1 612
- Forster RA, Cox LJ, Barrett RF, Booth TE, Briesmeister JF, Brown FB, Bull JS, Geisler GC, Goorley JT, Mosteller RD, Post SE, Prael RE, Selcow EC and Sood A 2004 MCNP™ Version 5 *Nucl Instruments Methods Phys Res Sect B Beam Interactions Mater Atoms* 213 82–6
- Gach HM, Tanase C and Boada F 2008 2D & 3D Shepp-Logan Phantom Standards for MRI 2008 19th Int Conf Syst Eng 521–6
- García-Pareja S, Lallena AM and Salvat F 2021 Variance-Reduction Methods for Monte Carlo Simulation of Radiation Transport *Aip Conf Proc* 9 718873
- Grogg KS, Toole T, Ouyang J, Zhu X, Normandin MD, Li Q, Johnson K, Alpert NM and Fakhri GE 2016 National Electrical Manufacturers Association and Clinical Evaluation of a Novel Brain PET/CT Scanner *J Nucl Med* 57 646–52 [PubMed: 26697961]
- Harrison RL, Vannoy SD, Haynor DR, Gillispie SB, Kaplan MS and Lewellen TK 1993 Preliminary Experience With The Photon History Generator Module Of A Public-domain Simulation System For Emission Tomography 1993 Ieee Conf Rec Nucl Sci Symposium Medical Imaging Conf 1154–8
- Hubbell JH and Seltzer SM 2004 Tables of X-Ray Mass Attenuation Coefficients and Mass Energy-Absorption Coefficients (version 1.4) Online: 10.18434/T4D01F
- Jan S, Santin G, Strul D, Staelens S, Assié K, Autret D, Avner S, Barbier R, Bardiès M, Bloomfield PM, Brasse D, Breton V, Bruyndonckx P, Buvat I, Chatziioannou AF, Choi Y, Chung YH, Comtat C, Donnarieix D, Ferrer L, Glick SJ, Groiselle CJ, Guez D, Honore P-F, Kerhoas-Cavata S, Kirov AS, Kohli V, Koole M, Krieguer M, Laan DJ van der, Lamare F, Largeton G, Lartizien C, Lazaro D, Maas MC, Maigne L, Mayet F, Melot F, Merheb C, Pennacchio E, Perez J, Pietrzyk U, Rannou FR, Rey M, Schaart DR, Schmidtlein CR, Simon L, Song TY, Vieira J-M, Visvikis D, Walle R V de, Wieërs E and Morel C 2004 GATE: a simulation toolkit for PET and SPECT *Phys Med Biol* 49 4543–61 [PubMed: 15552416]
- Lopes PC, Pinto M, Simoes H, Biegun AK, Dendooven P, Oxley DC, Parodi K, Schaart DR and Crespo P 2012 Optimization of collimator designs for real-time proton range verification by measuring prompt gamma rays 2012 Ieee Nucl Sci Symposium Medical Imaging Conf Rec Nss Mic 3864–70
- MacFarlane CR and Radiologists AC of 2006 ACR accreditation of nuclear medicine and PET imaging departments. *J Nucl Medicine Technology* 34 18–24
- Merlin T, Stute S, Benoit D, Bert J, Carlier T, Comtat C, Filipovic M, Lamare F and Visvikis D 2018 CASToR: a generic data organization and processing code framework for multi-modal and multi-dimensional tomographic reconstruction *Phys Medicine Biology* 63 185005
- Miller SR, Gaysinskiy V, Shestakova I and Nagarkar VV 2005 Recent advances in columnar CsI(Tl) scintillator screens *Penetrating Radiat Syst Appl Vii* 59230F–59230F–10
- O’Connell J and Bazalova-Carter M 2021 fastCAT: Fast cone beam CT (CBCT) simulation *Med Phys* 48 4448–58 [PubMed: 34053094]
- Paredes-Pacheco J, López-González FJ, Silva-Rodríguez J, Efthimiou N, Niñerola-Baizán A, Ruibal Á, Roé-Vellvé N and Aguiar P 2021 SimPET—An open online platform for the Monte Carlo

- simulation of realistic brain PET data. Validation for 18F-FDG scans *Med Phys* 48 2482–93 [PubMed: 33713354]
- Perl J, Shin J, Schümann J, Faddegon B and Paganetti H 2012 TOPAS: An innovative proton Monte Carlo platform for research and clinical applications *Med Phys* 39 6818–37 [PubMed: 23127075]
- Polster L, Schuemann J, Rinaldi I, Burigo L, McNamara AL, Stewart RD, Attili A, Carlson DJ, Sato T, Méndez JR, Faddegon B, Perl J and Paganetti H 2015 Extension of TOPAS for the simulation of proton radiation effects considering molecular and cellular endpoints *Phys Medicine Biology* 60 5053–70
- Poludniowski G, Landry G, DeBlois F, Evans PM and Verhaegen F 2009 SpekCalc : a program to calculate photon spectra from tungsten anode x-ray tubes *Phys Med Biol* 54 N433–8 [PubMed: 19724100]
- Rit S, Oliva MV, Brousmiche S, Labarbe R, Sarrut D and Sharp GC 2014 The Reconstruction Toolkit (RTK), an open-source cone-beam CT reconstruction toolkit based on the Insight Toolkit (ITK) *J Phys Conf Ser* 489 012079
- Rogers DWO, Faddegon BA, Ding GX, Ma C-M., We J and Mackie T 1995 BEAM: A Monte Carlo code to simulate radiotherapy treatment units *Med Phys* 22 503–24 [PubMed: 7643786]
- Salvadori J, Labour J, Odille F, Marie P-Y, Badel J-N, Imbert L and Sarrut D 2020 Monte Carlo simulation of digital photon counting PET *Ejnmmsi Phys* 7 23
- Sardari D, Maleki R, Samavat H and Esmaeeli A 2010 Measurement of depth-dose of linear accelerator and simulation by use of Geant4 computer code *Reports Pract Oncol Radiotherapy* 15 64–8
- Schuemann J, McNamara AL, Ramos-Mendez J, Perl J, Held KD, Paganetti H, Incerti S and Faddegon B 2018 TOPAS-nBio: An Extension to the TOPAS Simulation Toolkit for Cellular and Sub-cellular Radiobiology *Radiat Res* 191 125–38
- Shepp LA and Vardi Y 1982 Maximum Likelihood Reconstruction for Emission Tomography *Ieee T Med Imaging* 1 113–22
- Shi M, Myronakis M, Hu Y-H, Jacobson M, Lehmann M, Fueglistaller R, Huber P, Baturin P, Wang A, Ferguson D, Harris T, Morf D and Berbeco R 2019 A novel method for fast image simulation of flat panel detectors *Phys Medicine Biology* 64 095019
- Spiga J, Siegbahn EA, Bräuer-Krisch E, Randaccio P and Bravin A 2007 The GEANT4 toolkit for microdosimetry calculations: Application to microbeam radiation therapy (MRT) *Med Phys* 34 4322–30 [PubMed: 18072497]
- Thing RS, Bernchou U, Mainegra-Hing E, Hansen O and Brink C 2016 Hounsfield unit recovery in clinical cone beam CT images of the thorax acquired for image guided radiation therapy *Phys Medicine Biology* 61 5781
- Wettenhovi V-V, Vauhkonen M and Kolehmainen V 2021 OMEGA—open-source emission tomography software *Phys Medicine Biology* 66 065010
- Wrońska A 2020 Prompt gamma imaging in proton therapy - status, challenges and developments *J Phys Conf Ser* 1561 012021
- Zarifi M, Guatelli S, Bolst D, Hutton B, Rosenfeld A and Qi Y 2017 Characterization of prompt gamma-ray emission with respect to the Bragg peak for proton beam range verification: A Monte Carlo study *Phys Medica* 33 197–206
- Zhu H, Chen Y, Sung W, McNamara AL, Tran LT, Burigo LN, Rosenfeld AB, Li J, Faddegon B, Schuemann J and Paganetti H 2019 The microdosimetric extension in TOPAS: development and comparison with published data *Phys Medicine Biology* 64 145004



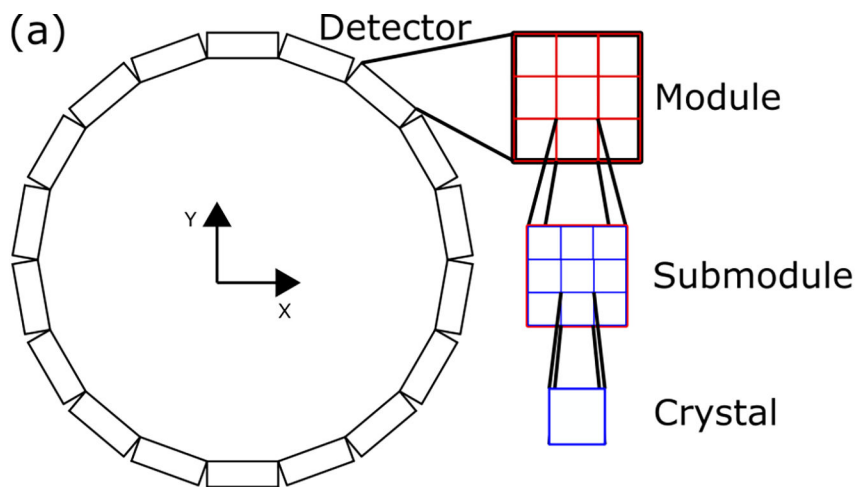
**Figure 1.** Schematic diagram of the class hierarchy of TOPAS-imaging extension. (a) hierarchy for Imager geometries. (b) Hierarchy for PET, SPECT, and PG scorers. The scorers inherit from TsNTuple scorer for digitization and list-mode output. They store detected signals in Pulse and use Digitizers to reject unwanted signals. (c) Hierarchy for a CBCT scorer. The CBCT scorer uses binned scorer to accumulate signals per pixel and obtain 2D projection data. The solid black arrows depict the inheritance relationship, and the dashed diamond arrows depict composite relationship between classes.



**Figure 2.**

Schematic diagram of a flat-panel detector (a) cross-sectional view and (b) frontal view.

The gray boxes and circles depict scintillating crystals and the red boxes and circles around them are reflective layers. (c) TOPAS Parameter Control File for a flat-panel detector. The character before the colon depicts the type of the variable, the Ge means that the parameters are for geometry components. Red-colored strings are the name of variables.



```

(b)
#===== Ring imager =====
s:Ge/PETImager/Type           = "RingImager"
s:Ge/PETImager/Parent         = "World"
d:Ge/PETImager/RingRadius     = 173.25 mm
i:Ge/PETImager/NbOfDetectors  = 21
s:Ge/PETImager/Material       = "Air"

#===== Defining crystals =====
s:Ge/PETImager/Crystal/Material = "LYSO"
d:Ge/PETImager/Crystal/HLX      = 1.168835 mm
d:Ge/PETImager/Crystal/HLY      = 10 mm
d:Ge/PETImager/Crystal/HLZ      = 1.168835 mm
i:Ge/PETImager/Crystal/NbOfXBins = 22
i:Ge/PETImager/Crystal/NbOfYBins = 1
i:Ge/PETImager/Crystal/NbOfZBins = 22
d:Ge/PETImager/Crystal/XGap      = 0 mm
d:Ge/PETImager/Crystal/ZGap      = 0 mm

#===== Defining collimator =====
b:Ge/PETImager/Collimator/Exists = "True"
s:Ge/PETImager/Collimator/Material = "G4_w"
s:Ge/PETImager/Collimator/OpeningMaterial = "Air"
d:Ge/PETImager/Collimator/HL      = 10 mm
u:Ge/PETImager/Collimator/XSeptaThicknessPercentage = 0.2
u:Ge/PETImager/Collimator/ZSeptaThicknessPercentage = 0.2

#===== Defining modules =====
i:Ge/PETImager/Module/NbOfXBins = 1
i:Ge/PETImager/Module/NbOfYBins = 1
i:Ge/PETImager/Module/NbOfZBins = 4
d:Ge/PETImager/Module/XGap      = 0 mm
d:Ge/PETImager/Module/ZGap      = 0 mm

#===== Defining submodules =====
i:Ge/PETImager/Submodule/NbOfXBins = 1
i:Ge/PETImager/Submodule/NbOfYBins = 1
i:Ge/PETImager/Submodule/NbOfZBins = 1
d:Ge/PETImager/Submodule/XGap      = 0 mm
d:Ge/PETImager/Submodule/ZGap      = 0 mm

```

**Figure 3.**

(a) A schematic diagram of the ring-shaped detector. The detector is constructed with hierarchic structures composed of crystals, submodules, modules, and detectors. (b) TOPAS Parameter Control File for a ring-shaped detector.

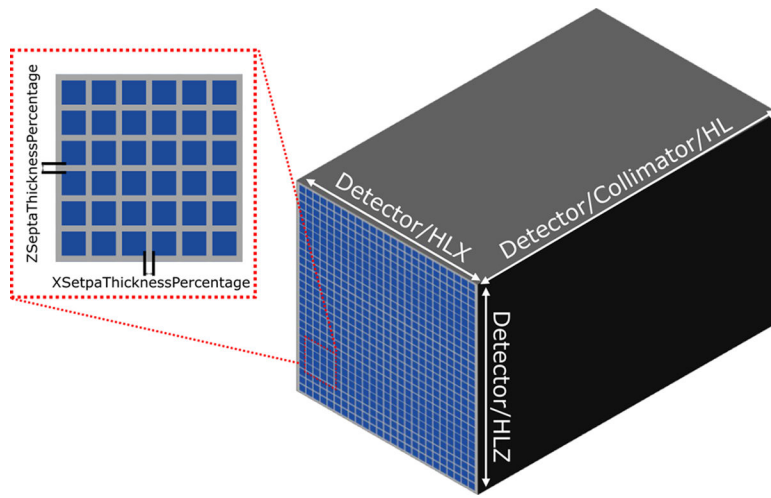


**Figure 4.** 2-D array type parallel-hole collimator. The collimator has the same sizes as the detector, and the number of holes in the collimator is the same as the number of crystals in the detector.

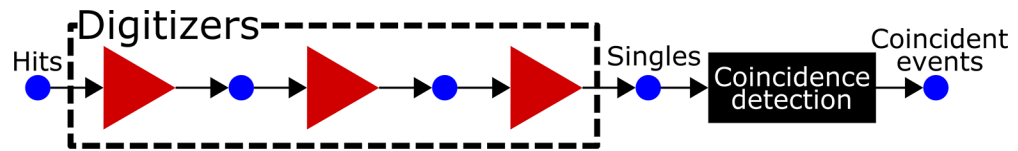


**Figure 5.** Digitizer chain of the PET scorer. Signals detected in a PET detector (hits) go through the digitizers (red triangles) selected by users. Coincident signals (coincident events) are detected among the digitized signals (singles).

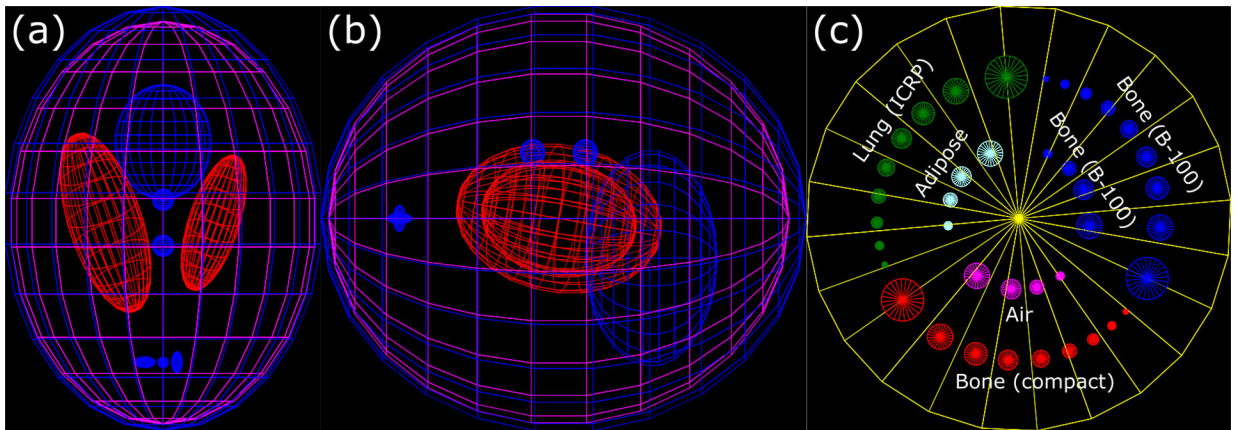


**Figure 6.** Modified 3D Shepp-Logan phantom (a) top-view and (b) lateral-view. (c) Top-view of modified contrast phantom.

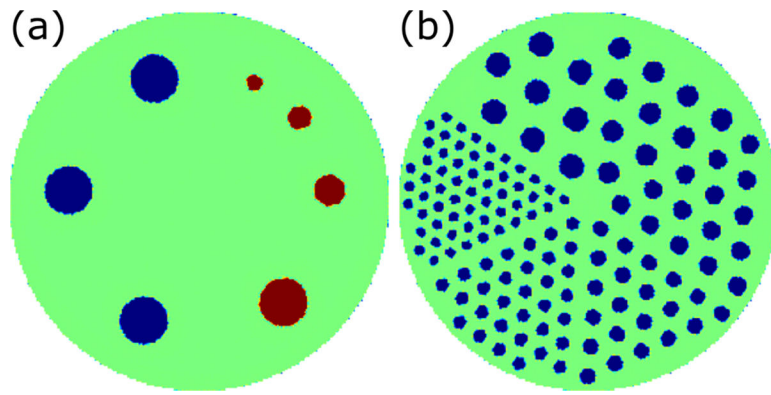


**Figure 7.** Cross-sectional slices of ACR-type phantom (a) contrast part and (b) resolution part.

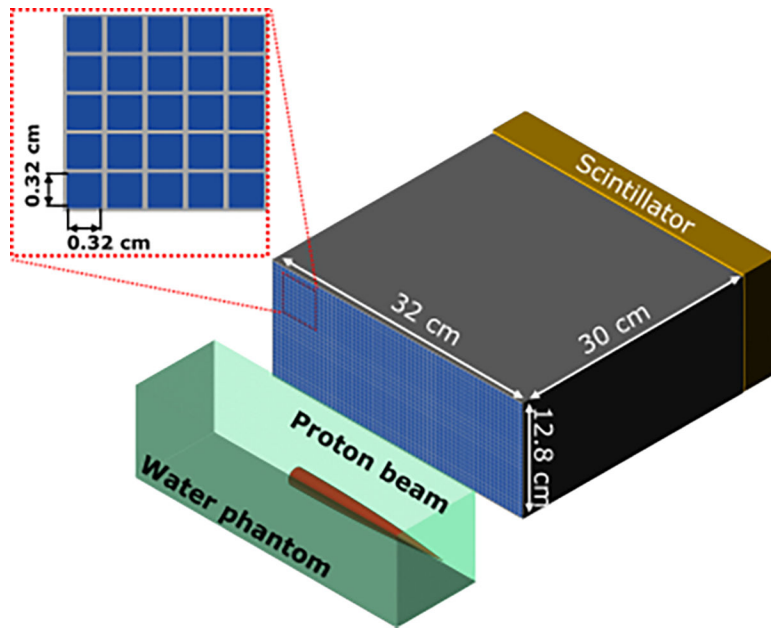


**Figure 8.**  
PG detector system with collimator and water phantom

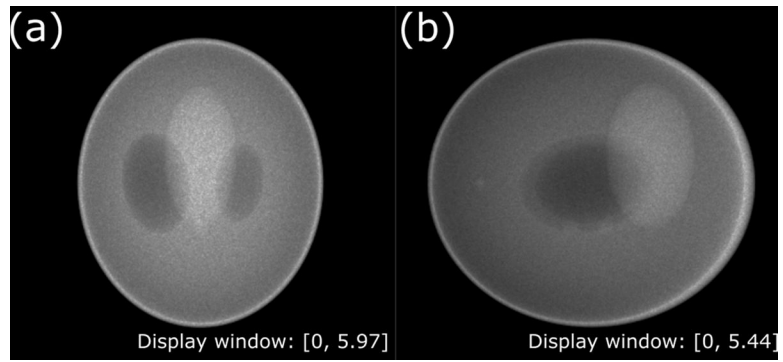


**Figure 9.** Projection data of the modified Shepp-Logan phantom. Projection angle: (a) 0 deg and (b) 90 deg



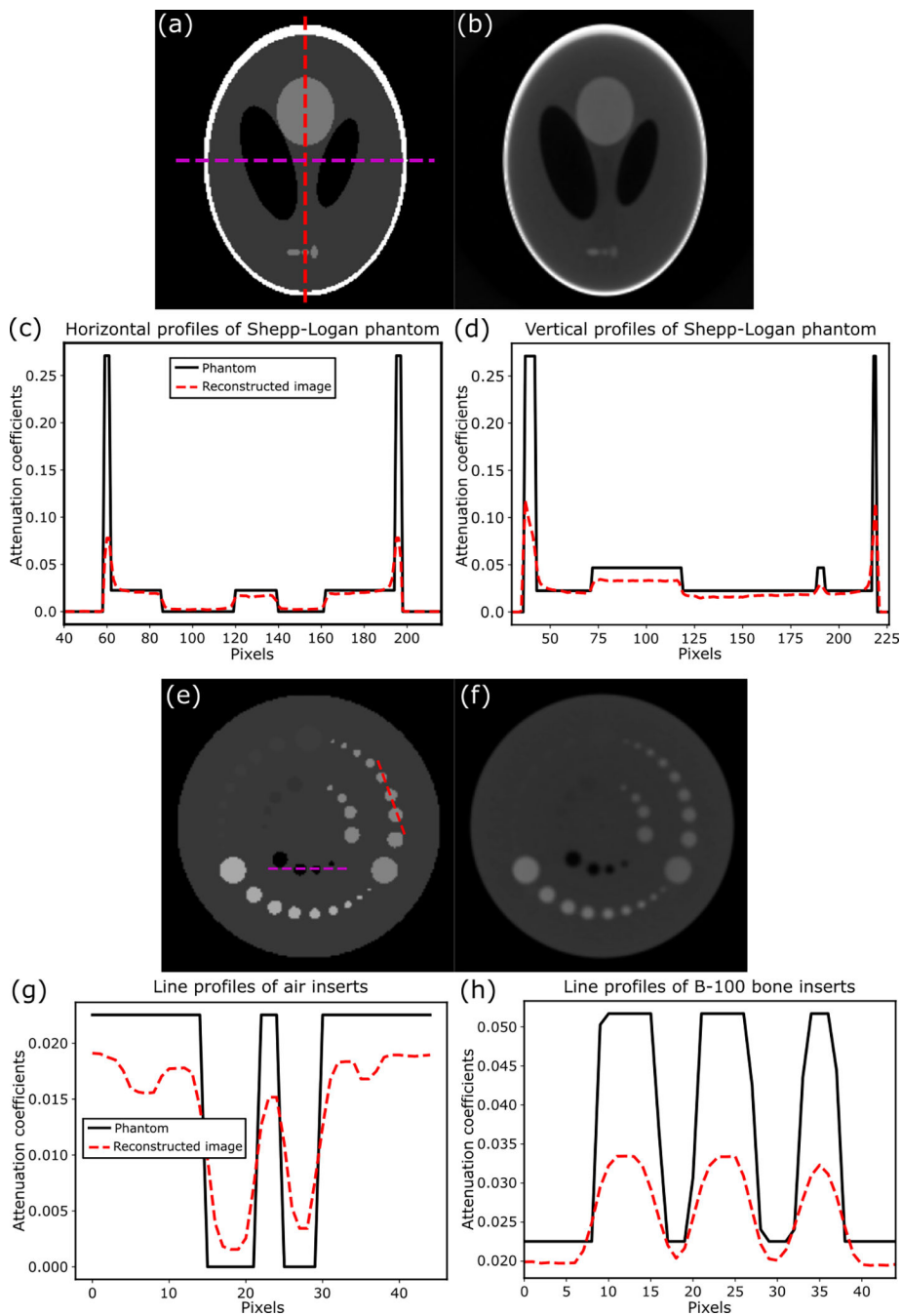


**Figure 10.** Central slice of (a) the numerical Shepp-logan phantom and (b) reconstructed volume. Display window: [0, 0.1]. Line profiles of the (c) magenta-dashed line and (d) red-dashed line in (a). Central slice of (e) the numerical contrast phantom and (f) reconstructed volume. Display window: [0, 0.1]. Line profiles of the (g) red-dashed line and (e) magenta-dashed line in (f).

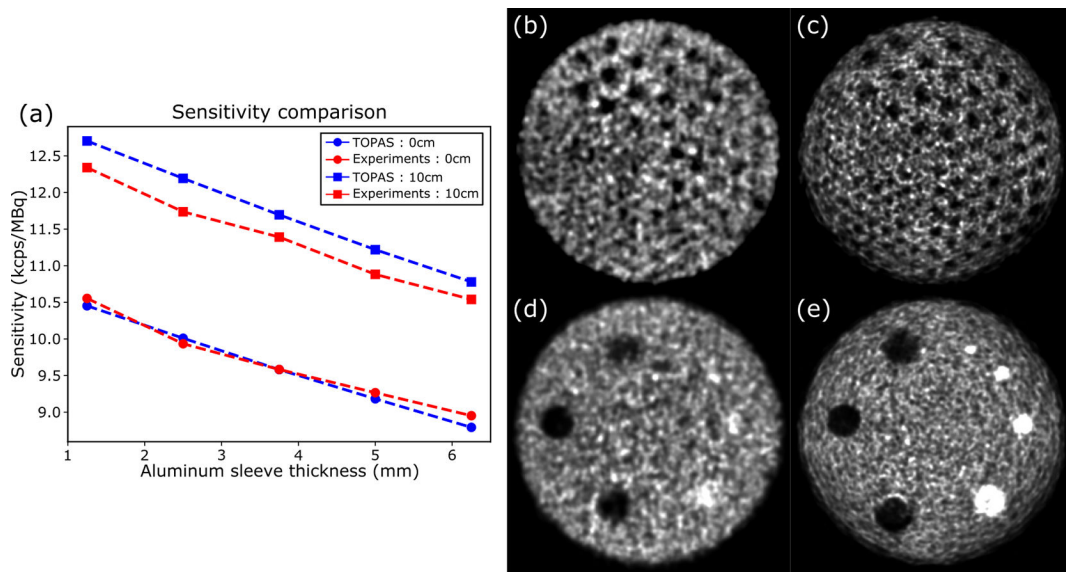


**Figure 11.**

(a) Sensitivity comparison results of the NeuroPET/CT system. Resolution section of the ACR phantom obtained from (b) experimental system and (c) TOPAS simulations. Contrast section from the ACR phantom obtained from (d) experimental system and (e) TOPAS simulation.

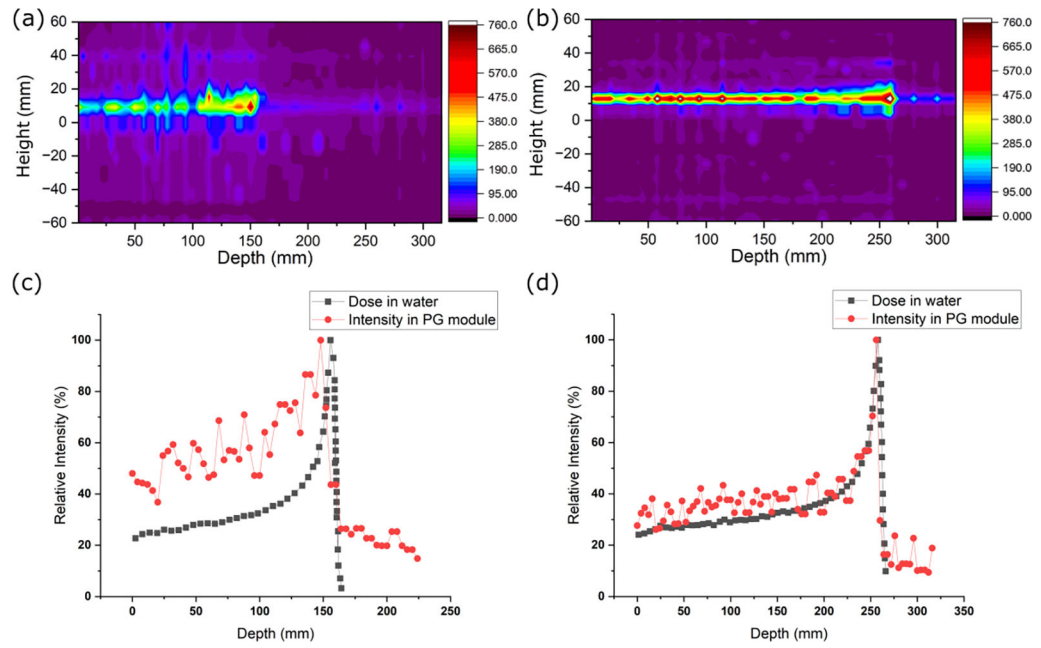


**Figure 12.** Measured data from PG for (a) 150 MeV and (b) 200 MeV protons. The line profiles of proton beams (square black) and measured intensity from PG system (circle red) for (c) 150 MeV and (d) 200 MeV protons.

**Table I.**

CBCT scanning geometry and corresponding TOPAS parameter names in TOPAS Parameter Control Files

Parameters	TOPAS parameter names	Values
Source-to-isocenter distance	BeamPosition/TransZ	1000 mm
Source-to-detector distance	BeamPosition/TransZ - CBCTImager/TransZ	1500 mm
Angular sampling	-	0.2237 deg / view
Detector pixel size	(2*CBCTImager/Crystals/HLX*CBCTImager/Crystals/NbOfXBins)/ (CBCTImager/XBins) * (2*CBCTImager/Crystals/HLZ*CBCTImager/Crystals/NbOfZBins)/(CB CTImager/ZB ins)	0.338 * 0.338 mm <sup>2</sup>
# of detector pixels	CBCTImager/PhotoDetector/XBins* CBCTImager/PhotoDetector/ZBins	1024 * 1024
Energy spectrum	XRay/BeamEnergySpectrumValues and XRay/ BeamEnergySpectrumWeights	120 kVp (0.1 mm Cu, 2mm Al)
Field of view	-	229.22 mm
# of primary particles	Xray/NumberOfHistoriesInRun	500x 10 <sup>6</sup>

**Table II.**

Composition of the Shepp-Logan phantom

	<b>Position (x, y, z) (cm)</b>	<b>Half-axis (a, b, c) (cm)</b>	<b>Material</b>
<b>Phantom outer shell</b>	(0, 0, 0)	(6.9, 8.1, 9.2)	Calcium oxide
<b>Phantom body</b>	(0, 0, 0.184)	(6.624, 7.8, 8.74)	Water
<b>Ellipsoid # 1</b>	(2.2, 0.0, 0.0)	(1.1, 2.2, 3.1)	Air
<b>Ellipsoid # 2</b>	(-2.5, 0.0, 0.0)	(1.6, 2.8, 4.1)	Air
<b>Ellipsoid # 3</b>	(0.0, -1.5, -3.5)	(2.1, 4.1, 2.5)	Teflon
<b>Ellipsoid # 4</b>	(0.0, 2.5, -1.0)	(0.46, 0.5, 0.46)	Teflon
<b>Ellipsoid # 5</b>	(0.0, 2.5, 1.0)	(0.46, 0.5, 0.46)	Teflon
<b>Ellipsoid # 6</b>	(-0.8, 0.0, 6.05)	(0.46, 0.5, 0.23)	Teflon
<b>Ellipsoid # 7</b>	(0.0, 0.0, 6.06)	(0.23, 0.2, 0.23)	Teflon
<b>Ellipsoid # 8</b>	(0.6, 0.0, 6.05)	(0.23, 0.2, 0.46)	Teflon

**Table III.**

PET scanning geometry and corresponding TOPAS parameter names in TOPAS Parameter Control Files

Parameters	TOPAS parameter names	Values
# of crystals per block	PETImager/Crystal/NbOfXBins* PETImager/Crystal/NbOfZBins	22 * 22
# of blocks per detector	PETImager/Module/NbOfXBins* PETImager/Module/NbOfZBins	1 * 4
# of detector	PETImager/NbOfDetectors	21
Size of crystals	(2* PETImager/Crystal/HLX) * (2* PETImager/Crystal/HLZ)	2.3 * 2.3 mm <sup>2</sup>
Thickness of crystals	2* PETImager/Crystal/HLY	20 mm
Axial FOV	-	250 mm
Transaxial FOV	-	220 mm
Crystal material	PETImager/Crystal/Material	LYSO:Ce
Energy window	PETScorer/Digitizer/EnergyCutoff/Threshold ~ PETScorer/Digitizer/EnergyCutoff/Uphold	400 ~ 650 keV
Prompt coincidence window	PETScorer/CoincidenceTimeWindowPrompts	10 ns
Random coincidence window	PETScorer/CoincidenceTimeDelayRandoms	1000 ns
Timing resolution	PETScorer/Digitizer/TimeResolution	500 ps